GEOFIZIKA VOL. 38 2021

DOI: https://doi.org/10.15233/gfz.2021.38.6
Original scientific paper

Properties of the Zagreb 22 March 2020 earthquake sequence – analyses of the full year of aftershock recording

Marijan Herak [1], Davorka Herak [1] and Nikša Orlić [2]

[1] Department of Geophysics, Faculty of Science, University of Zagreb, Zagreb, Croatia

[2] Geolux d.o.o., Samobor, Croatia

Received 23 August 2021, in final form 23 October 2021

Although strong and damaging earthquakes have hit Zagreb in the past, the 22 March 2020 earthquake (M_w 5.4) is the first one that was recorded by a modern digital local seismic network, and which could be analysed not only by macroseismic methods, but also by microseismic ones. Herewith we used the 3003 carefully analysed and located events from the first year of the aftershock sequence to learn more about the aftershock rate decay, their magnitude distribution, focal mechanisms and hypocentral locations. The aftershock activity rate was found to closely follow the modified Omori law, and fault-plane solutions for 10 events indicated prevailing pure-reverse faulting. Our analyses suggest that the reverse North Medvednica boundary fault (NMBF) was the causative fault, as it fits with the focal mechanisms and with the geometry of aftershock locations. The epicentral area was of a triangular shape with the mainshock in one vertex, and the opposite side of the triangle lying parallel to the surface trace of the NMBF. The hypocentres of aftershocks were predominantly located in the hanging wall of the fault. No surface break was observed, so the rupture is assumed to be buried. These facts were interpreted as a combination of the effect of conservation of mass (seismic flow) requiring some fault-parallel stress redistribution and transfer of material, and the fault loading and activation in the compressive environment controlled by the stress partition at the brittle-ductile transition zone within the crust. The later process involves compression within the hanging wall during the interseismic stage when the fault segment in the brittle crust is locked, followed by sudden dilatation during the rupture phase.

Keywords: Zagreb earthquake, causative fault, focal mechanisms, aftershock sequence

1. Introduction

The damaging Zagreb earthquake of 22 March 2020 (M_L 5.5, M_w 5.4) caused a loss of a life and large damage to building stock and infrastructure (estimated

at over 10 billion EUR). It reminded the citizens of Zagreb (and indeed of all Croatia) that earthquakes are the hazard we need to live with, and that calamities seldom come alone. This Chinese proverb sounds so true given that Croatia had to endure two damaging earthquakes in the time span of only 10 months (the M_w 6.4 Petrinja earthquake occurred on 29 December of the same year), and all of it during the COVID-19 pandemic and lockdown (more on preliminary seismological analyses and response of Croatian seismologists may be found in *e.g.* Dasović et al., 2020, Markušić et al., 2020, Šavor-Novak et al., 2020). But, the earthquake shouldn't have come as a surprise, as the seismicity around Zagreb is well known, the Great Zagreb 1880 earthquake is often publicly talked and written about (*e.g.* Herak and Herak, 2006), and this region is clearly recognized on the Croatian earthquake hazard map as the one characterized by high seismic hazard (Herak et al., 2011). However, the last significant earthquake shook Zagreb in 1906, and the notion of earthquake danger slowly seeped out of public concern during 114 years since.

As Fig. 1 shows, the Croatian Earthquake Catalogue (Herak et al, 1996; updated in 2020; CEC hereafter) lists several strong historical events in the

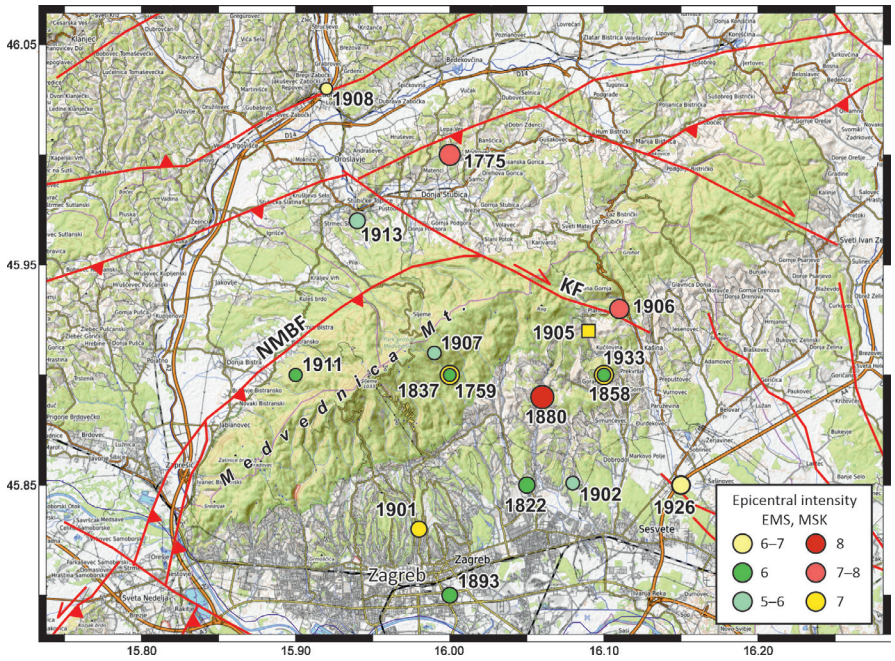

Figure 1. Epicentres of historical earthquakes (1700–1920), with epicentral intensity of 5.5 EMS (or MSK) or larger (after CEC). Only mainshocks are shown, except for the 1905 event (yellow square), which has recently been identified by Herak et al. (2021) as the foreshock of the 1906 earthquake. Traces of main faults (red) are modified after Tomljenović and Csontos (2001). NMBF – North Medvednica boundary fault, KF – Kašina fault. Base-map from OpenTopoMap (https://opentopomap.org).

epicentral region of Medvednica Mt. By far the most important one is the damaging earthquake of 9 November 1880 (I_0 = 8.0 EMS; macroseismic magnitude M_m 6.1 after Herak et al., 2021; intensity in Zagreb I_{ZAG} = VIII EMS) with the epicentre about 10 km to the NE from the city centre. Worth mentioning is also the quake of 2 January 1906 (M_m 5.3, M_L 5.3; I_{ZAG} = VI–VII EMS), which seems to have been of a similar size as the recent March 2020 event (Herak et al., 2021).

The traces of main seismogenic faults in the greater Zagreb area are shown in Fig. 1 (and in all subsequent figures) modified after Tomljenović and Csontos (2001), who also present the seismotectonic framework of the Medvednica Mt. (see also *e.g.* Tomljenović et al. 2008). For the seismic hazard of Zagreb itself, two faults stand out – the reverse, SE-to-SSE dipping North Medvednica boundary fault (NMBF) and the right lateral Kašina strike-slip fault (KF).

Epicentres of historical events as shown in Fig. 1 are almost all found beneath SE slopes and foothills of the Medvednica Mt., in the block bounded by NMBF to the NW and KF to the NE. Given the poor accuracy of their locations, the positions of epicentres of pre-instrumental events could not confidently indicate causative fault(s) for any of the large historical earthquakes. Traditionally, and solely based on relatively large damage reported from small villages close to the Kašina fault, this fault was commonly quoted as the source for the 1880 earthquake (*e.g.* Prelogović and Cvijanović, 1981). It thus somehow became almost synonymous of the Zagreb seismogenic source, although already Gorjanović-Krambereger (1907) identified both faults (with an additional fault to the SE of Medvednica) as seismogenic sources. Only recently, Latečki et al. (2021) gave preference to the NMBF over KF for the 1880 earthquake based on comparison of theoretical realistic shaking scenarios for the city of Zagreb and the observed macroseismic field for the 1880 event.

As more instrumental data became available in the second half of the 20th century, a more complex picture started to emerge (Fig. 2). In particular, seismicity was found also beneath NW flanks of Medvednica, and under its SE part, as well as in the area between two strike-slip faults, to the NE and E of the KF. Most of the earthquakes were of small magnitude, but the Kraljev Vrh earthquake of 3 September 1990 reached M_L 5.0 and epicentral intensity of VII EMS (Markušić et al., 1993; Herak et al., 2021; see the symbol with thick outline in Fig. 2a). The Kraljev Vrh earthquake was the strongest instrumentally recorded one in the Medvednica area since the quake of 1906 (see more in Herak et al, 2021), until the 2020 earthquake occurred. Its epicentre lay close to NMBF, and rather far from KF. However, very sparse regional networks equipped with analogue instruments could not provide data of sufficient quality to reliably locate its aftershock sequence. Kraljev Vrh earthquake was also the first one in this area for which reported data allowed the focal mechanism solution (FMS) to be computed. It indicated a pure reverse dip-slip on a fault striking ENE–WSW,

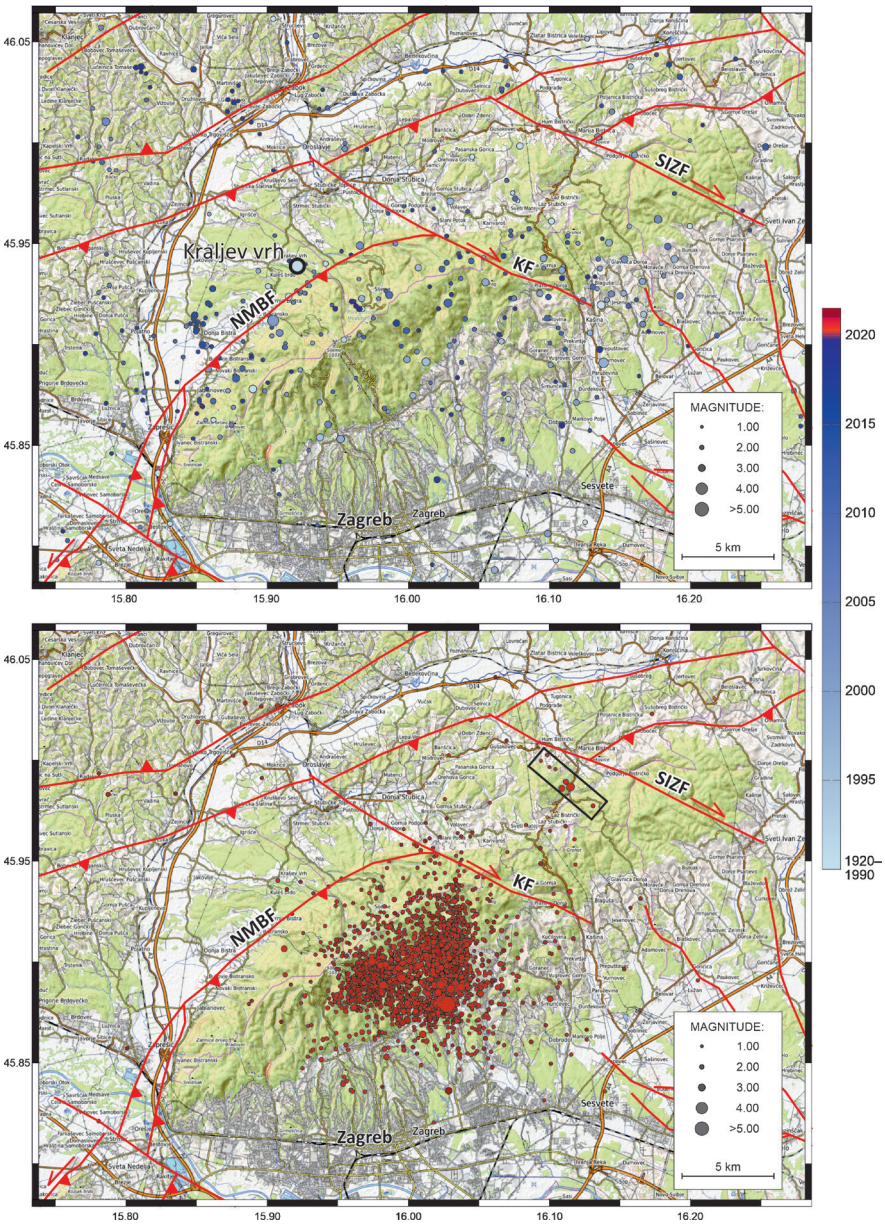

Figure 2. Epicentres of instrumentally recorded earthquakes: *a*) 1920–2019, $M_L \geq 1.0$; *b*) Zagreb 2020–2021 sequence, all magnitudes. The year of occurrence is indicated by the colour scale. NMBF – North Medvednica boundary fault, KF – Kašina fault, SIZF – Sveti Ivan Zelina fault. Traces of main faults (red) are modified after Tomljenović and Csontos (2001). The rectangle in part *b*) close to SIZF encloses the 8 possible foreshocks, 28 January–14 March 2020. Base-map from OpenTopoMap (https://opentopomap.org).

which together with the proximity of its epicentre to the NMBF, suggested it to be its seismogenic fault.

The 2020 Zagreb earthquake and its aftershock sequence provide seismologists and geoscientists the first opportunity for an in-depth study of an earthquake in the Medvednica epicentral zone using high-quality digital data. Herewith, we use the full first year of recordings to compile the representative earthquake catalogue, compute focal mechanism solutions (FMS) for 10 earthquakes of the series, analyse the magnitude distribution as well as the temporal evolution of the sequence, and draw conclusions on the causative fault and the faulting process.

2. Earthquake sequence of 2020–2021

The mainshock of the studied sequence occurred on 22 March 2020, and was followed by the strongest aftershock (M_L 4.9) 37 minutes later. However, 54 days earlier, on 28 January 2020 an M_L 3.3 earthquake occurred about 14 km to the NE from the future mainshock's epicentre, close to the mapped trace of the right lateral strike-slip Sveti Ivan Zelina fault (SIZF, Fig. 2). Its FMS (see section 2.3. below) indeed indicates a strike-slip mechanism with one of the solutions pointing to the vertical, NW–SE striking dextral fault, so we conclude that SIZF is the most probable source. The shock was followed by seven small aftershocks (M_L 0.1–2.4) aligned parallel to the SIZF (within the box in Fig. 2b). Whether this small sequence should be considered as foreshocks is debatable. On one hand, some declustering programs (*e.g.* Herak et al., 2009) will find them to be within the prescribed temporal and/or spatial windows for the M_L 5.5 mainshock, so they should be counted as foreshocks. On the other hand, this small cluster is only loosely connected with the main cluster of aftershocks (Fig. 2b), and the causative faults seem to be different, so perhaps they should not be considered foreshocks. We shall not offer firm suggestion, but will consider both sequences.

2.1. Seismogram analyses and the data set

The earthquakes were recorded by all local and regional networks. The closest active stations that provided the bulk of data are shown in Fig. 3. The stations on the Croatian territory were operated by the Croatian Seismological Survey of the Department of Geophysics, Faculty of Science in Zagreb (network CR), whereas those in Slovenia (SL) are maintained by the Slovenian Environment Agency, Ljubljana. We also used data from the networks GE, GR, HU, IV, MN, NI, OE, OX, RF, SJ and Z3 as available on EIDA (2020–2021, see list of DOIs in References).

Shortly after the earthquake, the existing small network around Zagreb was expanded by adding three BB-stations (two of them with collocated accelero-

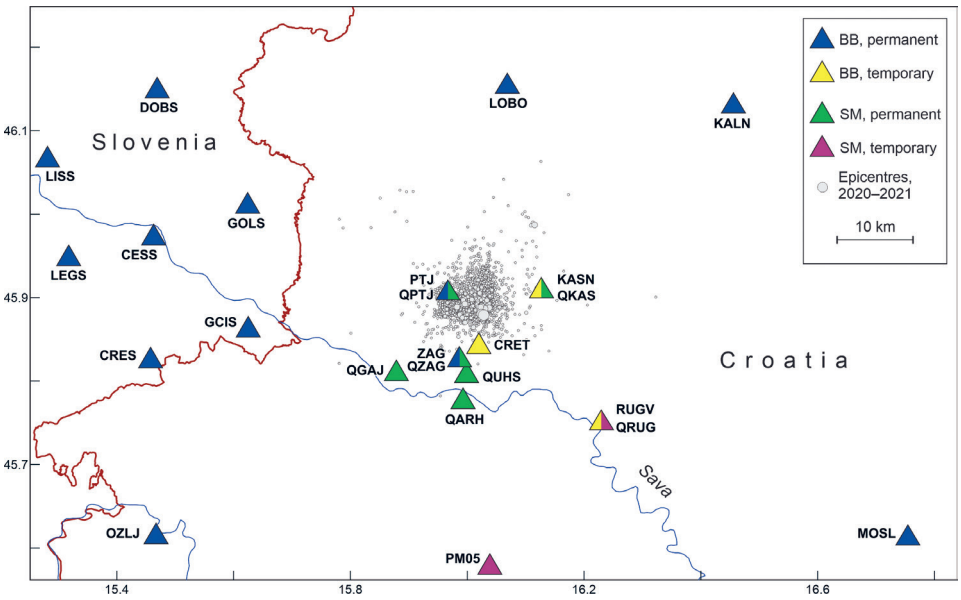

Figure 3. Permanent and temporary seismological stations closest to the epicentral area. BB – Broad-band stations; SM – Strong-motion stations.

graphs) to the area east and southeast of the epicentre, thus reducing the azimuthal gap. In January 2021 a temporary network was installed in the greater region of Petrinja (following the M_w 6.4 earthquake of 29 December 2020), which also provided some data for the last two months of the Zagreb sequence.

All available seismograms for the period 1 January 2020 – 22 March 2021 were analysed using the SANDI interactive seismogram analysis program (Orlić et al., 2005–2021) for phase-picking and data organization. Out of over 4000 earthquakes for which at least one phase could be confidently read, 3003 earthquakes provided enough good quality data to compute the magnitudes and locate their hypocentres. Locations for those 3003 events were based on a set of 41.845 phase onset times (25.477 Pg, 14.191 Sg, 1.531 Pn, 646 Sn) that were all hand-picked by an experienced analyst. The magnitudes computed are local magnitudes (M_L), estimated as described in detail by Herak (2020).

2.2. Magnitude distribution and temporal evolution of the aftershock sequence

Aftershock magnitude distribution is shown in Fig. 4, along with the fitted Gutenberg-Richter (GR) relation

$$\log N = a - bM_L.$$

Here N is the number of earthquakes with magnitude larger or equal to M_L (with $M_L \geq M_c$, M_c being the magnitude completeness threshold of the catalogue), and

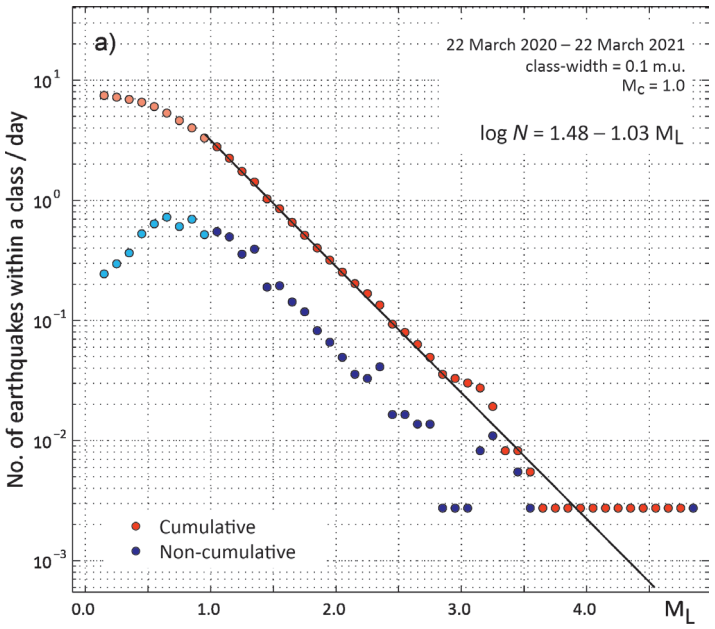

Figure 4. Cumulative (red) and non-cumulative (blue) magnitude distribution of the 22 March 2020 Zagreb earthquake aftershocks. Pale colours denote incomplete magnitude classes with a cut-off magnitude M_c = 1.0.

a and b are coefficients. Inspection of the observed magnitude distribution in Fig. 4 suggests M_c = 1.0. Fitting the GR relation to all $M_L \geq 1.0$, we obtain b = 1.03, a = 1.48.

The b-value of b = 1.03 is larger than b = 0.8–0.9 that is commonly assumed for the mainshocks in this area (*e.g.* Herak and Herak, 2009; Lee et al., 2013). Clear log-lin relationship shown in Fig. 4 suggests internal consistency of magnitudes.

The aftershock rate is modelled assuming validity of the modified Omori law,

$$n(t) = K / (t + c)^p,$$

where n is the number of aftershocks that occurred in the unit of time, K is the productivity that depends on the magnitude of the mainshock, t is time elapsed since the mainshock, c is a constant which shifts the time-scale in order to skip aftershocks that occurred too early in the mainshock's coda to be counted, and p is exponent usually close to p = 1.0. Figure 5 shows aftershock rates for events of magnitude $M_L \geq 1.5$ for the first year of the sequence, along with the fit of the modified Omori law (K = 37.00, c = 0.01 days, p = 1.02). Daily numbers of aftershocks were computed for consecutive 12 events (variable width of windows in time), with a shift of 6 events at a time. The cut-off magnitude was chosen above

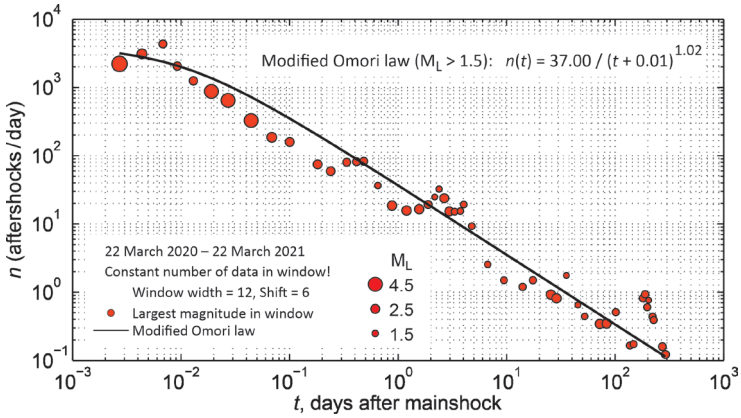

Figure 5. Decay of aftershock frequency with time (for earthquakes with $M_L \geq 1.5$). The line fitted is the modified Omori law $n(t) = K / (t + c)^p$.

the completeness threshold of this sequence to enable comparison with background seismicity rates in previous years.

The sequence productivity fell from about 3.000 aftershocks/day (or about 2 every minute) immediately after the mainshock, to about one such event every 10 days after a year had passed. According to CEC, the background rate within the aftershock zone for $M_L \geq 1.5$ during the last 10 years before the mainshock was about 5 such events/year, or 0.014 events/day. If the decay rate as shown in Fig. 5 persists, the earthquake activity would return to 'normal' about six years after the mainshock.

2.3. Focal mechanism solutions (FMS)

A set of hand-picked directions of the first P-phase motion on the vertical seismogram component from local and regional networks was used to invert for the best double-couple (BDC) focal mechanism solutions (FMS) for 10 events in the series using the methodology described by Herak et al. (2016). They are shown in Fig. 6, together with the BDC solutions for the three strongest events from moment tensor (MT) inversion, as published by international agencies.

The first motion polarity (FMP) solutions are generally similar to the BDC MT ones for the three events (Nos. 2, 3, 4) where both exist. All of them (except for the foreshock, No. 1 in Tab. 1 and Fig. 6) indicate reverse faulting, mostly on an ENE–WSW striking fault. The solutions for the two strongest events (Nos. 2 and 3) are similar and suggest a pure reverse rupture on a causative fault either dipping to the NNW or to the SSE. Our preferred solution, in line with the spatial distribution of hypocentres (see below, section 2.4) is the SSE-dipping fault, which corresponds by its dip and strike to the NMBF. Some of the small aftershocks indicate predominantly reverse faulting on small faults with different

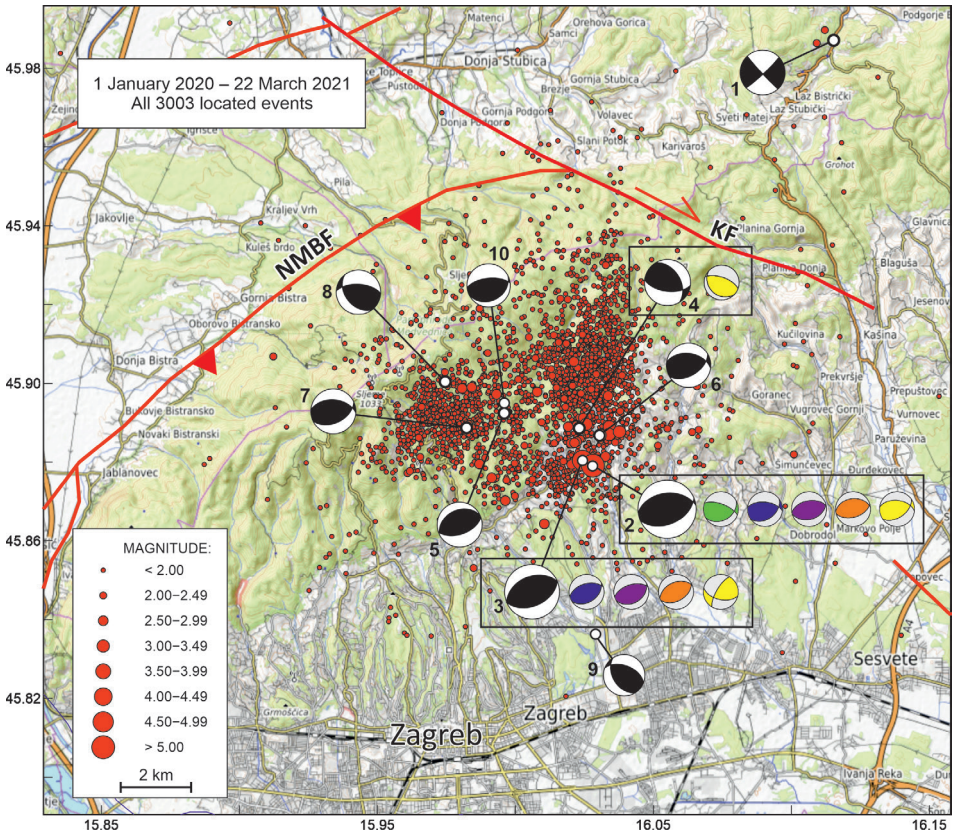

Figure 6. FMS for 10 events from the 2020–2021 Zagreb earthquake sequence. Best double-couple solutions are shown as lower hemisphere equal-area projection, with dilatational quadrants white. Authors are shown by the colour of the compressional quadrant: *Black* – FMP, first motion polarity solutions (this study). Moment tensor BDC solutions: *Purple* – GFZ, Geoforshungszentrum, Germany; *Orange* – USGS, United States Geological Survey, USA; *Yellow* – SLU, St. Louis University, USA; *Blue* – INGV, Istituto Nazionale di Geofisica e Volcanologia, Italy; *Green* – OCA, Observatoire de la Côte d'Azur, France. See the corresponding entries at the bottom of the References section for web links. The numbers next to each FMP beach-ball correspond to items in Tab. 1. Traces of main faults (red) are modified after Tomljenović and Csontos (2001). Base-map from OpenTopoMap (https://opentopomap.org).

strikes and/or dips (*e.g.* Nos. 4, 8, 9), which is indication of activation of smaller ruptures due to stress/strain redistribution within the hanging wall caused by the primary rupture.

2.4. Earthquake locations

Hypocentres were located by the latest version of the guided grid-search Hyposearch program (Herak, 1989), using a two-stage iterative scheme. Within

Table 1. Basic parameters for the 10 earthquakes with computed first-motion polarity FMS. φ, λ, δ are strike, dip and rake, respectively, and indices 1 and 2 denote the two nodal planes. Q is quality of solution (5 being the best, Herak et al. 2016), N_{pol} is number of polarities used.

No	Date	Time	Lat. N	Lon. E	*h*, km	M_L	$\varphi_1°$	$\delta_1°$	$\lambda_1°$	$\varphi_2°$	$\delta_2°$	$\lambda_2°$	Q/N_{pol}
1	28 Jan. 2020	07:53	45.987	16.115	4.5	3.29	137	87	–175	47	85	–2	5/49
2	22 Mar. 2020	05:24	45.879	16.028	10.1	5.50	67	47	79	263	44	102	5/147
3	22 Mar. 2020	06:01	45.880	16.024	9.4	4.87	67	47	89	248	43	91	4/137
4	22 Mar. 2020	06:41	45.889	16.023	8.8	3.46	97	59	57	329	44	132	3/55
5	23 Mar. 2020	10:12	45.892	15.996	7.3	3.28	245	35	85	71	55	93	3/33
6	24 Mar. 2020	19:53	45.887	16.031	8.6	3.20	59	51	63	278	46	119	3/60
7	23 Apr. 2020	07:52	45.889	15.982	9.3	3.29	65	47	69	274	47	111	4/55
8	17 Jun. 2020	15:51	45.900	15.975	6.3	3.21	273	61	61	142	40	131	3/65
9	1 Mar. 2021	08:19	45.836	16.029	8.8	2.79	291	51	65	148	45	118	3/39
10	20 Apr. 2021	21:15	45.895	15.996	9.0	3.05	63	29	71	264	63	100	3/53

this scheme, all locations are initially computed in stage 1, which is followed by computation of source-specific station corrections (SSSC) in stage 2 that are then subtracted from observed travel times. Iterations are repeated until the chosen misfit function stops decreasing. SSSCs are defined as average of observed travel-time residuals for each [station–phase–source volume] triplet. The source volume is determined for each triplet by the maximum distance (R_{max}) from the corresponding hypocentre as obtained in stage 1. In the case of the Zagreb aftershock sequence R_{max} = 2.0 km was used, and three iterations were needed to stabilize solutions.

To solve the forward problem of computing theoretical travel-times the program uses selected 1-D velocity model with horizontal layering, but first-order corrections for the head-waves travel times considering Moho topography are also applied. The locations and origin times in each location run depend on the velocity model, as well as on the choice of program control parameters – in our case the weights assigned to each reading, which depend on: phase and distance, azimuthal gap (γ) around each station, and individual travel-time residuals; the selected maximum distance R_{max} for SSSC computation; the choice of the misfit-function (least absolute values or least squares); and the rules for automatic replacement of the reported phase with the first-arriving one.

The SSSCs do not only reduce the systematic influence of local conditions below each station, but also limit the impact of spatial variation of observed travel times with respect to the theoretical ones for the chosen 1-D velocity model (*e.g.* Richards-Dinger and Shearer, 2000; Nooshiri et al., 2017; Nooshiri, 2019). Therefore, as long as the model is capable of predicting travel times that

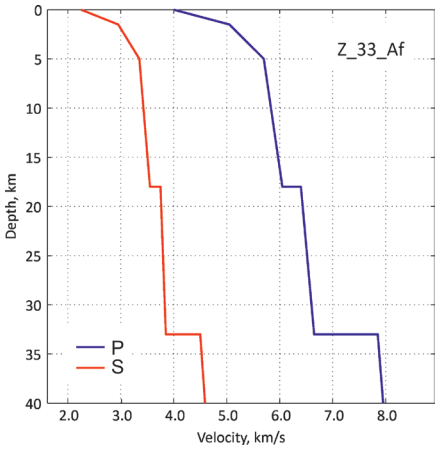

Figure 7. Velocity model Z_33_Af used for earthquake location in the Medvednica epicentral area.

are reasonably close to the true ones, the locations obtained using SSSCs will be more accurate and robust, and less dependent on the chosen model. Nevertheless, different velocity models and diverse control parameters will inevitably result in different sets of locations, even if the corresponding measures of goodness of fit do not change significantly. The influence of such epistemic variability of input data is beyond the scope of this study.

The model used to compute theoretical arrival times was derived from the model routinely used for earthquake location in the wider epicentral area of Medvednica, by slightly adjusting velocities in the upper crust above 18 km in order to make average residuals for Pg and Sg phases lower than 0.1 s without application of SSSCs. It is shown in Fig. 7.

Final locations were obtained after three iterations of locations and SSSC computation. Some statistical measures of the overall results are: mean traveltime residual $\langle \Delta t \rangle = 0.000$ s, mean absolute residual $\langle |\Delta t| \rangle = 0.093$ s, mean station correction $\langle \mathrm{SSSC} \rangle = -0.016$ s, mean absolute station correction $\langle |\mathrm{SSSC}| \rangle = 0.158$ s, and scaled median absolute deviation SMAD = 0.083 s. Confidence limits for hypocentral coordinates are defined by the 3D shape of the normalized misfit function in the coordinate space, at the level equal to the value of the inverse cumulative F-distribution with $(4, n - 4)$ degrees of freedom (n is number of onset times used to calculate the location) at the chosen confidence level (0.683, or 1σ, in our case). Fig. 8 presents distributions of data and results, while Fig. 9 shows examples of SSSCs for the three selected stations.

The histograms in Fig. 8 show that a large majority of earthquakes fell within the reporting network (station azimuthal gap, $\gamma < 180°$). Most of data come from less than 50 km away from the epicentre. 1σ-confidence limits for depths are, expectedly, larger than those for the epicentral position (but still

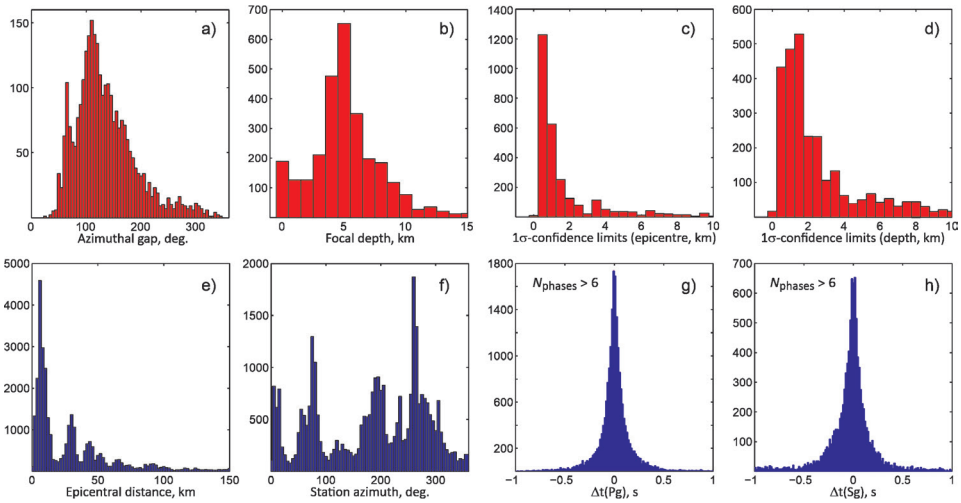

Figure 8. Histograms of quantities related to individual earthquakes (red, a–d), and those related to the dataset (blue, e–h). *a*) Distribution of the station azimuthal gaps; *b*) Distribution of focal depths, km; *c*) and *d*) Distribution of 1σ-confidence intervals for the epicentral coordinates and the depth, respectively, in km; *e*) Distribution of epicentral distances, km; *f*) Distribution of station azimuths; *g*) and *h*) Distribution of residuals for the Pg-phase and the Sg-phase, respectively, for events with more than 6 reported phases.

rather small, given the small number of stations close by), and distributions of residuals are quite narrow, symmetric, and centred around zero.

Figure 9 demonstrates how important SSSCs are, and how variable they may be even at short distances. The three stations shown (KASN, PTJ, and ZAG; yellow triangles in Fig. 9) are relatively close one to another, but the pattern of their SSSC is quite different. For KASN nearly all corrections are close to zero both for Pg and Sg phases. For PTJ they are mostly either negative (especially for Sg, and for earthquakes in the SE part of the aftershock area where the velocity model predicts too long traveltimes) or small, whereas for ZAG the velocity model seems to be too fast resulting in predominantly positive corrections, except for the events in the western-most part of the aftershock zone wherefrom the modelled travel-times are accurate. This spatial variability of station corrections is caused by lateral inhomogeneities throughout the upper crust; however, an in-depth analysis of the causes of spatial distribution of SSSCs as obtained here is beyond the scope of this study.

The final locations are shown in Fig. 10. Majority of epicentres lie on the SE slopes of Medvednica Mt., between the creeks of Bliznec and Vidovec. The confidence ellipses semimajor axes (*A*) are mostly shorter than 1 km (Fig. 10a). Epicentres form a fan-like triangular shape, with the base of the isosceles triangle lying about 4 km to the SE and in parallel to the surface trace of the NMBF,

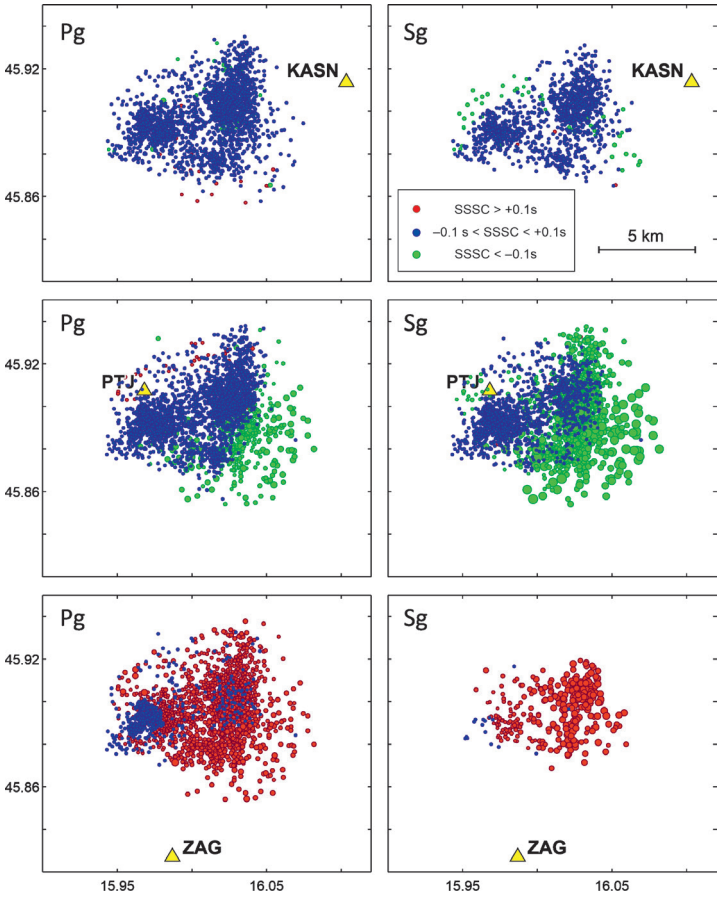

Figure 9. Source specific station corrections (SSSC) for stations KASN, PTJ and ZAG. The symbol denoting SSSC is plotted at the epicentre of each earthquake located using either Pg (*left*), or Sg phase (*right*) from the corresponding station. The size of the symbol scales with the SSSC.

whereas the mainshock is close to the opposite vertex of the triangle (Fig. 10a). The area of such a triangle, covering 85% of aftershocks, is about 50 km^2. A circle with radius of 9 km (area of 254 km^2) covers 98% of located aftershocks. Fig. 10b shows the depth distribution on a subsample containing only well constrained locations (*i.e.* those with at least 9 reported onset-times, with the azimuthal station gap less than 150° and the standard error of the epicentral location less than 1.5 km). It suggests that the focal depth in general increases with the distance from NMBF surface trace, and reaches no more than about 12 km. One can also notice that small and shallow events are grouped in two densely populated, but loosely connected groups in the western and northern part of the epicentre cluster (green boxes in Fig. 10b).

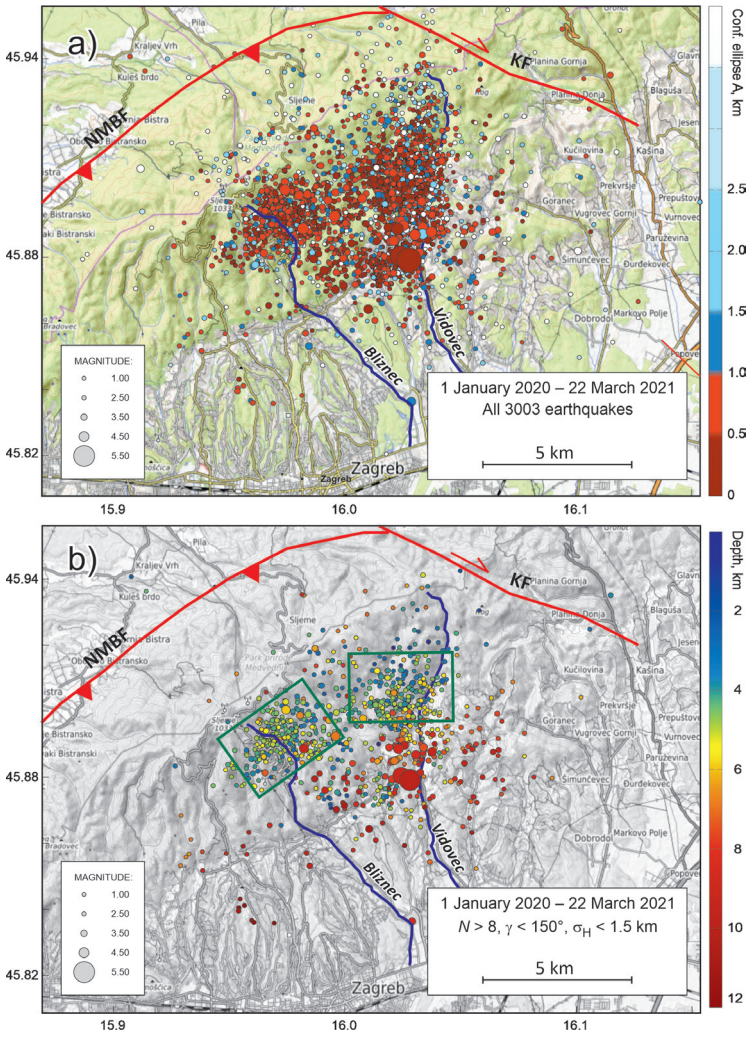

Figure 10. Final locations of the 2020–2021 Zagreb sequence. *a*) All 3003 events. The magnitude is shown by the size of a symbol, and the colour indicates the length of the semimajor axis of the 1σ error-ellipse. *b*) Epicentres of events with well constrained locations. Green boxes outline two distinct groups of predominantly small and shallow aftershocks. Symbol colour indicates focal depth according to the colour scale to the right. Traces of main faults (red) are modified after Tomljenović and Csontos (2001). Base-maps from OpenTopoMap (https://opentopomap.org).

Figure 11 presents the cross-section positioned orthogonally to the strike of the causative fault according to the FMS (Fig. 6 and Tab. 1), and passing through the mainshock's epicentre. To avoid crowding, only the most reliably located events are shown. The chosen corridor width is rather large (±2.5 km around the section trace) in order to capture overall positions of foci.

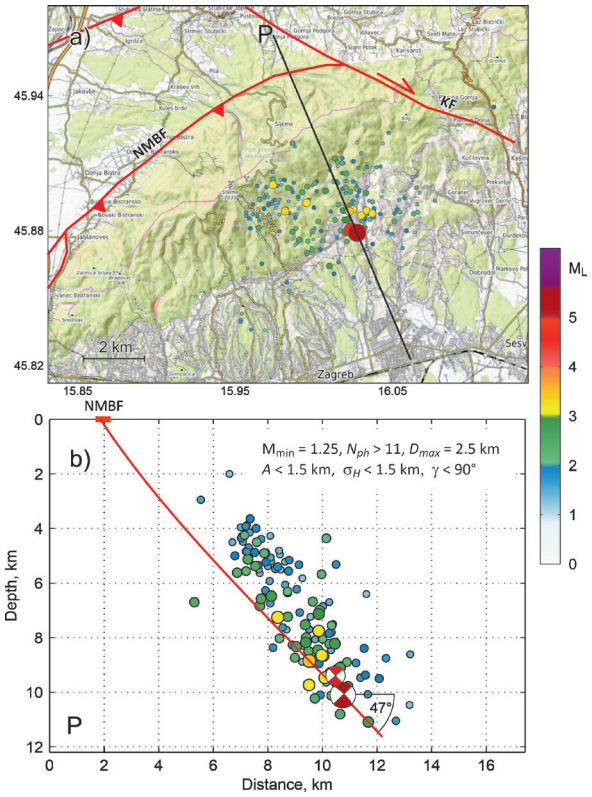

Figure 11. *a*) Map view of location of the cross-section P through the mainshock epicentre drawn perpendicularly to the strike of 67° as indicated by the FMS solution for the mainshock. Considered are only events satisfying criteria in the legend (M_{min} – the lowest magnitude, N_{ph} – number of reported phase onset times, A – semimajor axis of the error ellipse for the epicentral location, σ_H – standard error of the depth, γ – station azimuthal gap); *b*) Cross-section P, showing only events from part a) within the corridor ±2.5 km around the section trace. The symbol size and colour indicate magnitude according to the colour scale. The crossing of the profile with the NMBF surface trace is shown as short thick red line. Thin red line is a suggested trace of the NMBF fault in the cross-section, with the dip of 47° at the depth of the mainshocks' hypocentre, in agreement with the FMS (see Tab. 1). FMS for the mainshock and the largest aftershock are shown as projection onto the vertical focal hemisphere as seen from WSW (perpendicularly to the cross-section).

The projection of foci onto the cross-section P is shown in Fig. 11b. The hypocentres clearly suggest that the causative fault plane dips to the SSE at an angle of 45°–50°. The up-dip projection of the hypocentre cloud cuts the surface close to the suggested surface trace of the NMBF. This is a very strong indication that NMBF is indeed the fault that caused the Zagreb 2020 earthquake. Interpretation of the fault plane as shown in Fig. 11b suggests that most of aftershocks (at least those from the subset shown in Fig. 11) occurred within the hanging wall, up to as much as 2 km above the fault plane itself.

To see if this conclusion also holds for smaller events and for the complete length of the activated fault segment, we constructed a series of 8 parallel cross-sections, as shown in Figs. 12 and 13. Their orientation is chosen to be roughly perpendicular to the average strike of the NE section of the NMBF. The criteria for events to be included are relaxed compared to the ones used in cross-section P, as listed in the figure legend. The corridor width is now ±1 km. The cross-sections A–H through the cloud of hypocentres are shown in Fig. 13. The schematized side view of the NMBF is shown in all subplots as a thin dashed red line. The first two profiles (A, B) show only few, westernmost events, but they are well aligned with the assumed intersection of NMBF and the vertical profile plane. Starting with the profile C, in all subsequent cross-sections a large majority of aftershocks is found in the hanging wall, in a wedge-like volume enclosed between the fault plane and the two boundaries depicted as thick red dashed lines in Fig. 13. The upper, north-eastern boundary of this volume is sharp and is found 6–7 km down-dip from the surface, at the depth of 4–5 km. It may represent a secondary antithetic conjugate fault (AF in Fig. 13) dipping to the NW. As the profiles C, D and E show, nearly all aftershocks from the westernmost aftershock subgroup (see Fig. 10b) are found in a tight space between the fault plane and the upper wedge boundary (AF). The fault and the hanging wall to

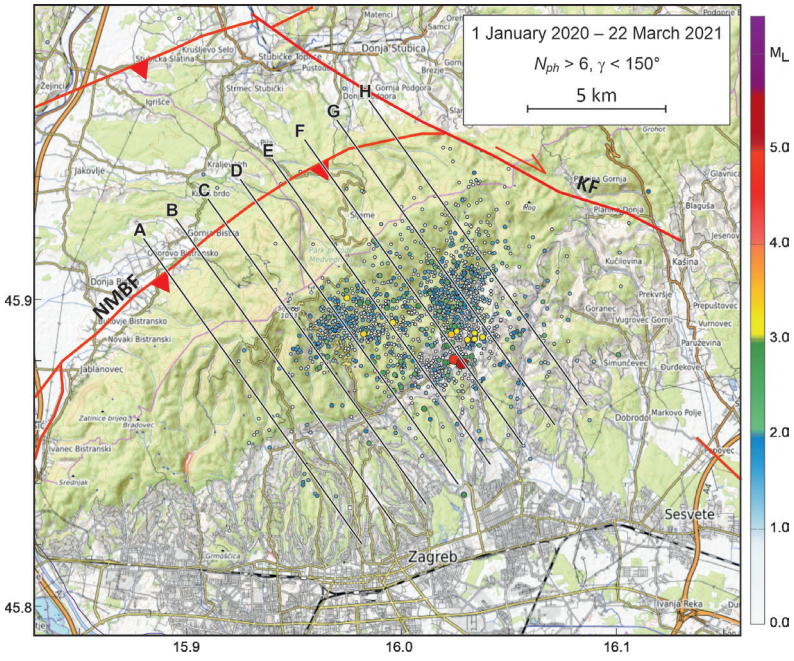

Figure 12. Map view of the 8 parallel cross-sections A–H across the NMBF and through the cloud of epicentres. Profiles are 1.3 km apart.

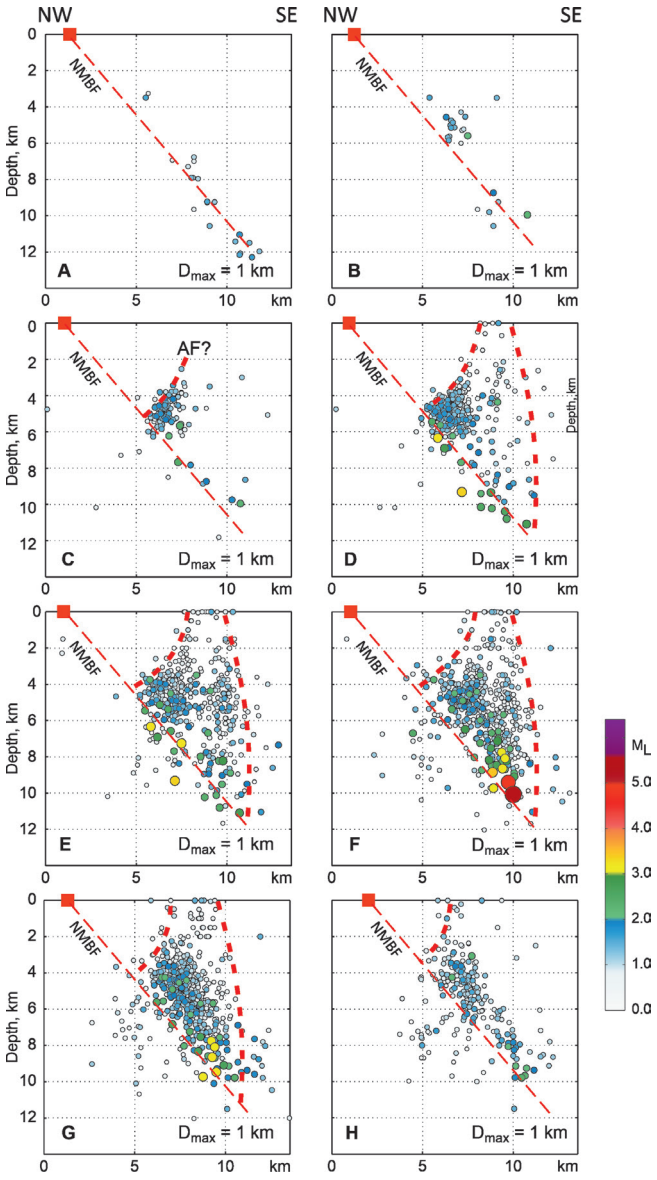

Figure 13. Cross-sections A–H from Fig. 12 showing hypocentres of earthquakes satisfying selection criteria (see Fig. 12), and located within ±1.0 km from the respective profile. Schematized position and trace of the NMBF is shown by thin-dashed red line, presuming that its dip does not significantly change along its strike (red square is the position of the intersection of surface trace of NMBF with the plane of the profile). Thick-dashed red curves enclose the bulk of foci within the hanging wall. AF in part C shows possible secondary antithetic fault.

the NE from the AF boundary remained practically aseismic. The southwestern margin of the activated wedge-like part of the hanging wall connects the surface and the fault-plane at the depth of 11–12 km (Fig. 13D–G). It is more diffuse but still well defined, sub-vertical and slightly downward convex. It should be noted that all earthquakes stronger than about M_L 3.0 are located along and close to the assumed fault plane.

3. Discussions

Observation that most aftershocks occur within the hanging wall is not uncommon with reverse or thrust seismogenic faults. It was reported, for instance by Unruh et al. (1997) for the Northridge earthquake (1994, California, USA); by Gahalaut et al. (2004) for the Jabalpur earthquake (1997, India); by Carena et al. (2002) and Chang et al. (2007) for the Chi-Chi earthquake (1999, Taiwan); by Zhang et al. (2010) for the Wenchuan earthquake (2008, Sichuan, China); by Fang et al. (2013) and Zhang et al. (2016) for the Lushan earthquake (2013, China); by Bai et al. (2015) for the Gorkha earthquake (2015, Nepal); and by Li et al. (2019) for the Osaka earthquake (2018, Japan).

In their paper on the M_w 6.7 Northridge earthquake, Unruh et al. (1997, their Fig. 2), also show that the aftershock epicentres formed a triangular zone, with geometrical properties that very much resemble the case of the Zagreb earthquake of 2020 (Fig. 10), but on a larger scale. They explain it by a kinematic model (their Figs. 5 and 9) applicable to blind or buried faults (Hudnut et al., 1996; Shen et al., 1996, Wald et al, 1996) in which "…coseismic slip on the blind Northridge thrust imposes a shortening on the hanging wall block in the direction of slip. The elastic response of the crust to the fault-normal shortening is a fault-parallel lengthening, which creates components of motion out of the plane that contains the slip vector. ...". In other words, since the fault did not break the surface, in shallow depths near the top of rupture the "conservation of volume may require out-of-plane or fault-parallel transfer of material". Such type of deformation accommodated by brittle fracture in aftershocks is referred to by Kostrov (1974) as *seismic flow* (also known as *cataclastic flow* in structural geology).

This fault-parallel movement was actually observed by the GPS stations in the vicinity of the Northridge rupture zone (Unruh et al., 1997). In the Zagreb case, such measurements are not available, and given the large difference in magnitude, the expected surface motions would be small. However, as surface break was not observed anywhere we may assume a buried rupture, and the model of fault-parallel lengthening and stress redistribution remains plausible for explanation of the peculiar shape of the aftershock zone for the Zagreb 2020 earthquake sequence.

The role of the brittle-ductile transition (BDT) zone within the crust on fault activation was studied by Doglioni et al. (2011; see also Doglioni et al., 2014, 2015). BDT zone marks the boundary of the seismogenic crustal layers usually at depths of 10–15 km. If a steady state strain rate is assumed in the ductile lower crust, stick-slip motion will result in the brittle upper crust depending on the capacity of active faults to temporarily store and then release accumulated elastic energy. Their modified model of fault loading and activation in a compressive tectonic environment (thrust and reverse buried faults) is schematically shown in Fig. 14.

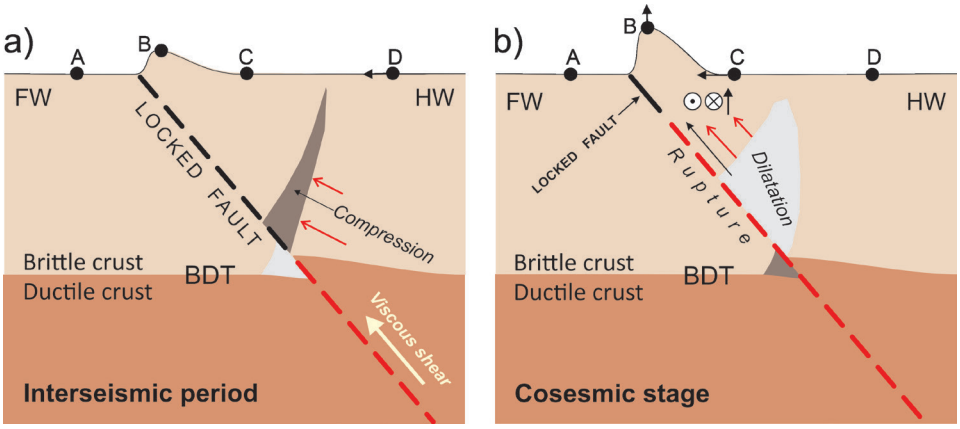

Figure 14. Model of fault loading and activation in compressive tectonic nvironment (Doglioni et al., 2011) modified for the case of buried rupture. *a*) Interseismic period; *b*) Coseismic stage. BDT is the brittle-ductile transition zone. A reverse fault (dashed line; black – locked; red – unlocked) crosses both crustal domains. HW – hanging wall, FW – foot wall. Modified after Doglioni et al. (2011, 2015).

According to Doglioni et al (2011), during the interseismic period a continuous viscous shear exists in the ductile layer, but the uppermost segment of the fault is locked (Fig. 14a). Consequently, an overcompressed volume (dark grey in Fig. 14a) in the hanging wall will build-up, separating the viscous shear from the locked fault plane above. During this stage, a portion of the footwall close to the BDT is expected to dilate (light-grey triangle in Fig. 14a; Doglioni et al., 2011, *e.g.* their Fig. 3). Once the locked fault (partly) yields and ruptures upwards during the coseismic stage (Fig. 14b), the compressed volume is suddenly dilated (light grey in Fig. 14b), and the part of the hanging wall above it is pushed towards the surface. In this process, conjugate antithetic faults may be created or activated in the shallow dilated part of the crust, forming triangular shapes similar to what is seen in cross-sections in Fig. 13 between the fault plane, the surface and the AF-boundary. Such observation for the case of the main thrusts at the front of the Apennines accretionary wedge in Italy is presented by Doglioni et al. (2015, their Fig. 5), and is also hinted at by the cross-sections published by Li et al. (2019) in the case of the Osaka M_w 5.5 earthquake of 2018.

However, if – as for the Zagreb mainshock – the rupture stopped before reaching the surface (possibly by the interaction with structural inhomogeneities, such as the aforementioned secondary antithetic fault), the coseismic surface deformation and uplift (point B in Fig. 14b) will be smaller than they would be if the rupture got to the surface (indeed, Govorčin, 2020, reported less than 4 cm maximum surface uplift according to his analyses of InSAR images). In such a case, as suggested above, the volume of the hanging wall in front of the dilata-

tion front will expand also sideways and parallel to the fault trace, which manifests itself as widening of the aftershock area close to the top of the rupture.

The process of stress redistribution during the coseismic dilatation phase is then likely to activate pre-existing small faults and cracks in this volume. Most of the aftershocks are thus expected to occur in the most-deformed part of the hanging wall – close to the rupture surface itself, and within the overcompressed-then-dilated volume of the hanging wall. This exact picture is seen in the case of the Zagreb 2020 earthquake series (Fig. 13), where larger aftershocks indeed prevail in the hanging wall close to the rupture plain, and the smaller ones tend to concentrate in the part of the hanging wall loosely delimited by the two red dashed lines that underwent coseismic dilatation. The triangular part of the hanging wall above it (where less stress redistribution is expected) seems to have remained practically aftershock-free in the process.

The structural interpretation of seismogenic fault(s) related to the 2020 Zagreb sequence was previously proposed by Markušić et al. (2020) who modelled two fault planes by fitting 3D-surfaces to routinely located hypocentres of the early aftershocks (257 events of the first 10 days, of which 122 were retained for analyses). They concluded that a system of two faults were active: Fault 1, a thrust dipping to the SE at an angle of 31° that produced the mainshock and the strongest aftershocks, and a steeply southward dipping Fault 2 of unspecified character that intersects Fault 1, and on which most of the small aftershocks occurred. The Fault 1 was modelled to reach the surface in the NW-hinterlands of Medvednica (about 5–10 km to the NE from our trace of the NMBF), whereas the surface trace of Fault 2 was estimated to pass near the summit of Medvednica, cutting the mountain body at an angle of about 30° from its long axis. Such interpretation is at odds with our analyses, which suggests rather simple rupture of the reverse NMBF dipping at 45–50°, with the general model of aftershocks occurring predominantly within the hanging wall of the NMBF. Such a notion actually prohibits *a priori* modelling of reverse/thrust fault planes by fitting surfaces through the clouds of hypocentres, as they may not cluster around the fault plane but above it.

4. Conclusions

One year of seismicity following the 22 March 2020 Zagreb earthquake (M_w 5.4) offered a golden opportunity to perform in-depth studies of an earthquake that caused substantial damage to the Croatian capital. Although strong earthquakes have hit Zagreb in the past, this is the first one that was recorded by a modern (albeit small) digital local seismic network, and which can be analysed not only by macroseismic methods, but also by microseismic ones. Herewith we used the 3003 carefully analysed and located events from the first year of the aftershock sequence to learn more about their rate decay with time, the magnitude distribution, focal mechanisms for the possible foreshock, mainshock and

aftershocks, and their hypocentral locations. The aftershock activity rate was found to closely follow the modified Omori law, and fault-plane solutions indicated prevailing pure-reverse faulting.

Our analyses suggest that the North Medvednica boundary fault (NMBF) was the causative fault – it fits with the focal mechanisms and with the geometry of aftershock locations. The rupture was buried, *i.e.* it did not reach the surface. During the first year of sequence epicentral area was of a triangular shape with the mainshock in one vertex, and the opposite side of the triangle lying parallel to the surface trace of the NMBF. The foci of aftershocks were predominantly found in the hanging wall of the NMBF. These facts were interpreted as a combination of the effect of conservation of mass (*seismic flow*) requiring some fault-parallel stress redistribution and transfer of material, and the fault loading and activation process in the compressive environment involving compression within the hanging wall during the interseismic stage when the fault segment in the brittle crust is locked, followed by sudden dilatation during the rupture phase.

Acknowledgements – This study was supported by Croatian Science Foundation project HRZZ-IP-2020-02-3960 – DuFAULT. We sincerely thank three anonymous referees and Bruno Tomljenović and Josip Stipčević, whose kind and thoughtful suggestions helped us to improve the manuscript.

References

Bai, L., Liu, H., Sistema, J., Mori, J., Zhang, T., Ishikawa, Y. and Li, G. (2016): Faulting structure above the Main Himalayan Thrust as shown by relocated aftershocks of the 2015 Mw 7.8 Gorkha, Nepal, earthquake, *Geophys. Res. Lett.*, **43**, 637–642, https://doi.org/10.1002/2015GL066473.

Carena, S., Suppe, J. and Kao, H. (2002): The active detachment of Taiwan illuminated by small earthquakes and its control of first-order topography, *Geology*, **30**, 935–938, https://doi.org/10.1130/0091-7613(2002)030<0935:ADOTIB>2.0.CO;2.

Chang, C.-H., Wu, Y.-M., Zhao, L. and Wu, T.-T. (2007): Aftershocks of the 1999 Chi-Chi, Taiwan, earthquake: The first hour, *B. Seismol. Soc. Am.*, **97**, 1245–1258, https://doi.org/10.1785/0120060184.

Dasović, I., Herak, D., Herak, M., Latečki, H., Mustać, M. and Tomljenović, B. (2020): O potresima u Hrvatskoj, *Vijesti Hrvatskoga geološkog društva*, **57**, 1, 4–27 (in Croatian).

Doglioni, C., Barba, S., Carminati, E. and Riguzzi, F. (2011): Role of the brittle-ductile transition on fault activation, *Phys. Earth Planet. In.*, **184**, 160–171, https://doi.org/10.1016/j.pepi.2010.11.005.

Doglioni, C., Barba, S., Carminati, E. and Riguzzi, F. (2014): Fault on-off versus coseismic fluids reaction, *Geosci, Front.*, **5**, 767–780, https://doi.org/10.1016/j.gsf.2013.08.004.

Doglioni, C., Barba, S., Carminati, E. and Riguzzi, F. (2015): Fault on-off versus strain rate and earthquakes energy, *Geosci. Front.*, **6**, 265–276, https://doi.org/10.1016/j.gsf.2013.12.007.

EIDA (2020–2021): *European Integrated Data Archive*, http://eida.gfz-potsdam.de/webdc3/ (last accessed 7 August 2021). Networks providing data:
CR – https://doi.org/10.7914/SN/CR; GE –http://doi.org/10.14470/TR560404;
GR – https://doi.org/10.25928/mbx6-hr74; HU – http://doi.org/10.14470/UH028726;
IV – https://doi.org/10.13127/SD/X0FXnH7QfY; MN – https://doi.org/10.13127/SD/fBBBtDtd6q;
NI – https://doi.org/10.7914/SN/NI; OE – https://doi.org/10.7914/SN/OE;

OX – https://doi.org/10.7914/SN/OX; RF – https://doi.org/10.7914/SN/RF; SJ – no DOI registered; SL – https://doi.org/10.7914/SN/SL; Z3 – https://doi.org/10.12686/alparray/z3_2015.

Fang, L., Wu, J., Wang, W., Lü, Z., Wang, Ch., Yang T. and Cai, Y. (2013): Relocation of the mainshock and aftershock sequences of MS7.0 Sichuan Lushan earthquake, *Chinese Sci. Bull.*, **58**, 3451–3459, https://doi.org/10.1007/s11434-013-6000-2.

Gahalaut, V. K., Rao, V. K. and Tewari, H. C. (2004): On the mechanism and source parameters of the deep crustal Jabalpur earthquake, India, of 1997 May 21: Constraints from aftershocks and changes in static stress, *Geophys. J. Int.*, **156**, 2, 345–351, https://doi.org/10.1111/j.1365-246X.2003.02140.x.

Gorjanović-Kramberger, K. (D.) (1907): Die geotektonischen Verhältnisse des Agramer Gebirges und die mit denselben im Zusammenhang stehenden Erscheinungen, *Physikalische Abhandlungen, Anhang zu den Abhandlungen der Königlich Preussischen Akademie der Wissenschaften, Berlin* (in German).

Govorčin, M. (@Govorcin) (2020): *Sentinel-1 coseismic interferogram of M5.3 and M4.8 #Zagreb #earthquake. #INSAR shows ~2.5 cm surface displacement. Coseismic deformation and GFZ moment tensor indicate the rupture on the North Medvednica fault. #ZagrebEarthquake #Croatia,1:50 PM, March 24*, 2020, tweet.

Herak, D. and Herak, M. (2006): Veliki zagrebački potres 1880. godine, *Meridijani*, studeni 2006, 4–13 (in Croatian).

Herak, D., Herak, M. and Tomljenović, B. (2009): Seismicity and earthquake focal mechanisms in North-Western Croatia, *Tectonophysics*, **465**, 212–220, https://doi.org/10.1016/j.tecto.2008.12.005.

Herak, M., Allegretti, I., Herak, D., Ivančić, I., Kuk, V., Marić, K., Markušić, S. and Sović, I. (2011): *Republika Hrvatska, Karta potresnih područja*, available at http://seizkarta.gfz.hr.

Herak, M. and Herak, D. (2009): Analyses of seismicity as input for earthquake hazard studies in Bosnia and Herzegovina, in*: Selected topics in earthquake engineering – from earthquake source to seismic design and hazard mitigation*, edited by Trifunac, M. Banja Luka, ZIBL, 1–26.

Herak, M., Herak, D. and Markušić, S. (1996): Revision of the earthquake catalogue and seismicity of Croatia, 1908–1992, *Terra Nova*, **8**, 86–94, https://doi.org/10.1111/j.1365-3121.1996.tb00728.x.

Herak, M., Herak, D. and Dasović, I. (2016): Fault-plane solutions and stress orientation in the greater region of Northern and Central Dinarides, *Book of Abstracts, 35th General Assembly of the European Seismological Commission*, 4–10 September 2016, Trieste, ESC2016-480.

Herak, M. (2020): Conversion between the local magnitude (M_L) and the moment magnitude (M_w) for earthquakes in the Croatian Earthquake Catalogue, *Geofizika*, **37**, 197–211, https://doi.org/10.15233/gfz.2020.37.10.

Herak, M., Herak, D. and Živčić, M. (2021): Which one of the three latest large earthquakes in Zagreb was the strongest – the 1905, 1906 or the 2020 one?, *Geofizika*, **38**, https://doi.org/10.15233/gfz.2021.38.5.

Hudnut, K. W., Shen, Z., Murray, M., McClusky, S., King, R., Herring, T., Hager, B., Feng, Y., Fang, P., Donnellan, A. and Bock, Y. (1996): Co-seismic displacements of the 1994 Northridge, California, earthquake, *B. Seismol. Soc. Am.*, **86**, No. 1B, S19–S36, https://doi.org/10.1785/BSSA08601B0S19.

Kostrov, V. V. (1974): Seismic moment and energy of earthquakes, and seismic flow of rock, *Izv. Acad. Sci. USSR Phys. Solid Earth*, English Translation, **1**, 23–44.

Latečki, H., Molinari, I. and Stipčević, J. (2021): 3D physics-based seismic shaking scenarios for city of Zagreb, Capital of Croatia, *B. Earthq. Eng.*, **19**, 12, 1–27, https://doi.org/10.1007/s10518-021-01227-5.

Lee, V., Herak, M., Herak, D. and Trifunac, M. (2013): Uniform hazard spectra in western Balkan Peninsula, *Soil Dyn. Earthq. Eng.*, **55**, 1–20, https://doi.org/10.1016/j.soildyn.2013.08.001.

Li, Y., Wang, D., Xu, S., Fang, L., Cheng, Y., Luo, G., Yan, B., Bogdan, E. and Mori, J. (2019): Thrust and conjugate strike-slip faults in the 17 June 2018 MJMA 6.1 (Mw 5.5) Osaka, Japan, earthquake sequence, *Seismol. Res. Lett.*, **90**, 6, 2132–2141, https://doi.org/10.1785/0220190122.

Markušić, S., Stanko, D., Korbar, T., Belić, N., Penava, D. and Kordić, B. (2020): The Zagreb (Croatia) M5.5 Earthquake on 22 March 2020, *Geosciences*, **10**, 252, https://doi.org/10.3390/geosciences10070252.

Nooshiri, N. (2019): SCOTER – Multiple-earthquake location by using Static and Source-Specific station Correction TERms, *Scientific Technical Report - STR Data*, **19/05**, Potsdam, GFZ German Research Centre for Geosciences, 31 pp, https://doi.org/10.2312/GFZ.b103-19056.

Nooshiri, N., Saul, J., Heimann, S., Tilmann, F. and Dahm, T. (2017): Revision of earthquake hypocentre locations in global bulletin data sets using source-specific station terms, *Geophys. J. Int.*, **208**, 2, 589–602, https://doi.org/10.1093/gji/ggw405.

Orlić, N., Herak, M. and Miklić, D. (2007–2021): *SANDI – Seismogram ANalysis and DIsplay,* computer program, Department of Geophysics, Faculty of Science, University of Zagreb.

Prelogović, E. and Cvijanović, D. (1981): Potres u Medvednici 1880. godine, *Geološki vjesnik*, **34**, 37–146 (in Croatian).

Richards-Dinger, K. B. and Shearer, P. M. (2000): Earthquake locations in southern California obtained using source-specific station terms, *J. Geophys. Res.*, **105**, 10939–10960.

Šavor Novak, M., Uroš, M., Atalić, J., Herak, M., Demšić, M., Baniček, M., Lazarević, D., Bijelić, N., Crnogorac, M. and Todorić, M. (2020): Potres u Zagrebu 22. ožujka 2020. – Preliminarni izvještaj o seizmološkim istraživanjima i oštećenjima zgrada (Zagreb earthquake of 22 March 2020 – Preliminary report on seismologic aspects and damage to buildings), *Građevinar*, **72**, 10, 843–867 (in Croatian and English).

Shen, Z.-K., Ge, B. X., Jackson, D. D., Potter, D., Cline, M. and Sung, L.-Y. (1996): Northridge earthquake rupture models based on the Global Positioning System measurements, *B. Seismol. Soc. Am.*, **86**, No. lb, S37–S48, https://doi.org/10.1785/BSSA08601B0S37.

Tomljenović, B. and L. Csontos (2001): Neogene-Quaternary structures in the border zone between Alps, Dinarides and Pannonian Basin (Hrvatsko zagorje and Karlovac Basins, Croatia), *Int. J. Earth Sci. (Geologische Rundschau)*, **90**, 560–578, https://doi.org/10.1007/s005310000176.

Tomljenović, B., Csontos, L., Marton, E. and Marton, P. (2008). Tectonic evolution of the northwestern Internal Dinarides as constrained by structures and rotation of Medvednica Mountains, North Croatia, in: *Tectonic aspects of the Alpine-Dinaride-Carpathian system*, edited by Siegesmund, S., Fuegenschuh, B. and Froitzheim, N. Bodmin, Cornwall, Geological Society London, 145–167.

Unruh, J. R., Twiss, R., J. and Hauksson, E. (1997): Kinematics of postseismic relaxation from aftershock focal mechanisms of the 1994 Northridge, California, earthquake, *J. Geophys. Res.*, **102**, No. B11, 24,589–24,603, https://doi.org/10.1029/97JB02157.

Wald, D. J., Heaton, T. H. and Hudnut, K. W. (1996): The slip history of the 1994 Northridge, California, earthquake determined from strong motion, teleseismic, GPS and leveling data, *B. Seismol. Soc. Am.*, **86**, No. 1b, S49–S70, https://doi.org/10.1785/BSSA08601B0S49.

Zhang, G., Hetland, E. A., Shan, X., Vallée, M., Liu, Y., Zhang, Y. and Qu, C. (2016): Triggered slip on a back reverse fault in the Mw 6.8 2013 Lushan, China earthquake revealed by joint inversion of local strong motion accelerograms and geodetic measurements, *Tectonophysics*, **672–673**, 24–33, https://doi.org/10.1016/j.tecto.2016.01.031.

Zhang, P.-Zh., Wen, X.-Z., Shen, Zh.-K. and Chen, J.-H. (2010): Oblique, high-angle, listric-reverse faulting and associated development of strain: The Wenchuan earthquake of May 12, 2008, Sichuan, China, *Annu. Rev. Earth Pl. Sc.*, **38**, 353–382, https://doi.org/10.1146/ANNUREV-EARTH-040809-152602.

GFZ – https://geofon.gfz-potsdam.de/eqinfo/form.php?lang=en (last visited 8 August 2021).

INGV – http://rcmt2.bo.ingv.it/ (last visited 8 August 2021).

OCA – http://sismoazur.oca.eu/focal_mechanism_emsc (last visited 8 August 2021).

SLU – http://www.eas.slu.edu/eqc/eqcmt.html (last visited 8 August 2021).

USGS – https://earthquake.usgs.gov/earthquakes/search/ (last visited 8 August 2021).

SAŽETAK

Svojstva niza potresa kod Zagreba nakon 22. ožujka 2020. godine – analiza prve godine zapisa naknadnih potresa

Marijan Herak, Davorka Herak i Nikša Orlić

Iako je Zagreb i u prošlosti doživio vrlo jake potrese, potres od 22. ožujka 2020. (M_w 5,4) prvi je koji je zabilježen suvremenom digitalnom lokalnom seizmičkom mrežom, te se mogao analizirati ne samo makroseizmičkim, već i mikroseizmičkim postupcima. U radu smo upotrijebili 3003 pažljivo analizirana i locirana potresa iz prve godine potresnoga niza kako bismo saznali više o opadanju učestalosti naknadnih potresa s vremenom, razdiobi njihovih magnituda, žarišnim mehanizmima i lokacijama hipocentara. Utvrđeno je da potresna aktivnost nakon glavnog potresa dobro slijedi Omorijev zakon, a žarišni mehanizmi za 10 potresa ukazuju na prevladavajuće reversno rasjedanje. Naše analize sugeriraju da su se glavni potres, kao i većina jačih naknadnih potresa dogodili na reversnom Sjevernom rubnom medvedničkom rasjedu. Epicentralno područje bilo je trokutastog oblika s glavnim potresom u jednom vrhu trokuta, dok je njegova suprotna strana ležala paralelno s površinskim tragom uzročnog rasjeda. Velika većina hipocentara naknadnih potresa nalazila se u krovini toga rasjeda. Kako nisu opažene pukotine na površini, pretpostavljeno je da se radi o pokrivenom rasjedu. Ove su činjenice protumačene kao kombinacija učinka očuvanja mase (seizmički tok) koji zahtijeva preraspodjelu napetosti paralelno s rasjednom plohom, te procesa aktiviranja rasjeda u kompresijskom tektonskom režimu. U tom modelu tijekom interseizmičkog razdoblja, dok je dio rasjeda u gornjoj (krtoj) kori 'zaključan', unutar njegova krovinskog krila dolazi do snažne kompresije, te do nagle dilatacije u krovini tijekom pucanja rasjeda.

Ključne riječi: zagrebački potres, uzročni rasjed, žarišni mehanizmi, niz potresa

Corresponding author's address: Marijan Herak, Department of Geophysics, Faculty of Science, University of Zagreb, Horvatovac 95, HR-10000 Zagreb, Croatia; e-mail: mherak@gfz.pmf.unizg.hr